11-1-2011

Infrared and upconversion spectroscopic studies of high Er3+content transparent YAG ceramic

M. Pokhrel

G. A. Kumar

P. Samuel

K. I. Ueda

T. Yanagitani

See next page for additional authors

Recommended Citation

M. Pokhrel, et. al., (2011) Infrared and upconversion spectroscopic studies of high Er3+content transparent YAG ceramic.Optical Materials Express1:71272. DOI: http://doi.org/10.1364/OME.1.001272

Infrared and upconversion spectroscopic studies of high Er^{3+}content transparent YAG ceramic

M. Pokhrel,[1] G. A. Kumar,[1] P. Samuel,[2] K. I. Ueda,[2] T. Yanagitani,[3] H. Yagi,[3] and D. K. Sardar[1,*]

[1]*Department of Physics and Astronomy, University of Texas at San Antonio, San Antonio, Texas 78249, USA*
[2]*Institute of Laser Science, University of Electro-communications, 1-5-1 Chofugaoka, Chofu-shi, Tokyo 182-8585, Japan*
[3]*Konoshima Takuma Works, Konoshima Chemical Co. Ltd., 80 Kouda, Mitoyo Kagawa 769-1103, Japan*
**dhiraj.sardar@utsa.edu*

Abstract: In this article, we report the detailed spectroscopic studies of high Er^{3+}content (50%) transparent YAG ceramic co-doped with nominal Cr^{3+} content (0.1 mol %). Various radiative and non-radiative spectroscopic properties such as radiative decay time, fluorescence branching ratio, emission/absorption cross sections, internal radiative quantum yields of the infrared and the upconverted emission bands are explored using standard experimental and theoretical methods and compared with YAG single crystal. Results show that although the non-radiative losses are high for 50% Er doped ceramic; several radiative spectral properties are almost in agreement with those for the single crystal YAG. Furthermore, because of the low dopant concentration of Cr^{3+}, the sensitizing effect of Cr^{3+} was not observed.

OCIS codes: (140.3613) Lasers, upconversion; (160.4670) Optical materials; (160.4760) Optical properties.

References and links

1. D. L. Chubb, A. Maria, T. Pal, M. O. Patton, and P. P. Jenkins, "Rare earth doped high temperature ceramic selective emitters," J. Eur. Ceram. Soc. **19**(13-14), 2551–2562 (1999).
2. T. Yanagitani, H. Yagi, and M. Ichikawa, "Production of yttrium-aluminum-garnet fine powder," Japanese Patent 10–101333 (1998).
3. G. A. Kumar, J. Lu, A. A. Kaminskii, K.-I. Ueda, H. Yagi, T. Yanagitani, and N. V. Unnikrishnan, "Spectroscopic and stimulated emission characteristics of Nd^{3+} in transparent YAG ceramics," IEEE J. Quantum Electron. **40**(6), 747–758 (2004).
4. M. Kaczkan, M. Borowska, K. Kolodziejak, T. Lukasiewicz, and M. Malinowski, "Intensity of optical transitions of Er^{3+} in $Yb_3Al_5O_{12}$ crystal," Opt. Mater. **30**(5), 703–706 (2008).
5. M. Eichhorn, S. T. Fredrich-Thornton, E. Heumann, and G. Huber, "Spectroscopic properties of Er^{3+}: YAG at 300–550 K and their effects on the 1.6 μm laser transitions," Appl. Phys. B **91**(2), 249–256 (2008).
6. J. X. Meng, K. W. Cheah, Z. P. Shi, and J. Q. Li, "Intense 1540 nm emission from Er doped Ce:YAG phosphor," Appl. Phys. Lett. **91**(15), 151107 (2007).
7. E. Georgiou, F. Kiriakidi, O. Musset, and J.-P. Boquillon, "1.65-μm Er:Yb:YAG diode-pumped laser delivering 80-mJ pulse energy," Opt. Eng. **44**(6), 064202–064212 (2005).
8. V. Lupei, A. Lupei, and A. Ikesue, "Transparent polycrystalline ceramic laser materials," Opt. Mater. **30**(11), 1781–1786 (2008).
9. D. Garbuzov, I. Kudryashov, and M. Dubinskii, "Resonantly diode laser pumped 1.6-μm-erbium-doped yttrium aluminum garnet solid-state laser," Appl. Phys. Lett. **86**(13), 131115 (2005).
10. W. Q. Shi, M. Bass, and M. Birnbaum, "Effects of energy transfer among Er^{3+} ions on the fluorescence decay and lasing properties of heavily doped $Er:Y_3AI_5O_{12}$," J. Opt. Soc. Am. B **7**(8), 1456–1462 (1990).
11. V. I. Zhekov, T. M. Murina, A. M. Prokhorov, M. I. Studenikin, S. Georgescu, V. Lupei, and I. Ursu, "Cooperative process in $Y_3Al_5O_{12}:Er^{3+}$ crystals," Sov. J. Quantum Electron. **16**(2), 274–276 (1986).
12. D. W. Chen, C. L. Fincher, T. S. Rose, F. L. Vernon, and R. A. Fields, "Diode-pumped 1-W continuous-wave Er:YAG 3-μm laser," Opt. Lett. **24**(6), 385–387 (1999).
13. J. Zhou, W. Zhang, L. Wang, Y. Shen, J. Li, W. Liu, B. Jiang, H. Kou, Y. Shi, and Y. Pan, "Fabrication microstructure and optical properties of polycrystalline $Er^{3+}:Y_3Al_5O_{12}$ ceramics," Ceram. Int. **37**(1), 119–125 (2011).

#150115 - $15.00 USD Received 30 Jun 2011; revised 12 Aug 2011; accepted 10 Oct 2011; published 17 Oct 2011

14. J. Zhou, W. Zhang, T. Huang, L. Wang, J. Li, W. Liu, B. Jiang, Y. Pan, and J. Guo, "Optical properties of Er, Yb co-doped YAG transparent ceramics," Ceram. Int. **37**(2), 513–519 (2011).
15. J. Zhou, W. Zhang, J. Li, B. Jiang, W. Liu, and Y. Pan, "Upconversion luminescence of high content Er-doped YAG transparent ceramics," Ceram. Int. **36**(1), 193–197 (2010).
16. G. Qin, J. Lu, J. Bisson, Y. Feng, K. Ueda, H. Yagi, and T. Yanagitani, "Upconversion luminescence of Er^{3+} in highly transparent YAG ceramics," Solid State Commun. **132**(2), 103–106 (2004).
17. L. Min, W. Shiwei, Z. Jian, A. Liqiong, and C. Lidong, "Preparation and upconversion luminescence of YAG:Er^{3+}:Yb^{3+} transparent ceramics," J. Rare Earths **24**(6), 732–735 (2006).
18. D. K. Sardar, C. C. Russell, J. B. Gruber, and T. H. Allik, "Absorption intensities and emission cross sections of principal intermanifold and inter-Stark transitions of $Er^{3+}(4f^{11})$ in polycrystalline ceramic garnet $Y_3Al_5O_{12}$," J. Appl. Phys. **97**(12), 123501 (2005).
19. T. Saiki, S. Motokoshi, K. Imasaki, H. Fujita, M. Nakatsuka, and C. Yamanaka, "Nd/Cr:YAG ceramic rod laser pumped using arc-metal-halide-lamp," Jpn. J. Appl. Phys. **46**(1), 156–160 (2007).
20. T. Saiki, K. Imasaki, S. Motokoshi, C. Yamanaka, H. Fujita, M. Nakatsuka, and Y. Izawa, "Disk-type Nd/Cr:YAG ceramic lasers pumped by arc-metal-halide-lamp," Opt. Commun. **268**(1), 155–159 (2006).
21. H. Yagi, T. Yanagitani, H. Yoshida, M. Nakatsuka, and K. Ueda, "Highly efficient flash lamp-pumped Cr^{3+} and Nd^{3+} co-doped $Y_3Al_5O_{12}$ ceramic laser," Jpn. J. Appl. Phys. **45**(1A), 133–135 (2006).
22. Z. J. Kiss and R. C. Duncan, "Cross-pumped Cr^{3+}/Nd^{3+} YAG laser crystal," Appl. Phys. Lett. **5**(10), 200–202 (1964).
23. R. Gross, G. Huber, B. Struve, and E. W. Duczinski, "Cr^{3+}-sensitization of the 3μm Er^{3+}:YAG laser," J. Phys. Colloq. **1**(7), C7.363–C7.366 (1991).
24. H. Stange, K. Petermann, G. Huber, and E. W. Duczynski, "Continuous wave 1.6 μm laser action in Er doped garnets at room temperature," Appl. Phys., B Photophys. Laser Chem. **49**(3), 269–273 (1989).
25. J. B. Gruber, J. R. Quagliano, M. F. Reid, F. S. Richardson, M. E. Hills, M. D. Seltzer, S. B. Stevens, C. A. Morrison, and T. H. Allik, "Energy levels and correlation crystal-field effects in Er^{3+}-doped garnets," Phys. Rev. B Condens. Matter **48**(21), 15561–15573 (1993).
26. Y. Yu, Z. Wu, and S. Zhang, "Concentration effects of Er^{3+} ion in YAG:Er laser crystal," J. Alloy. Comp. **302**(1-2), 204–208 (2000).
27. H. Xu, L. Zhou, Z. Dai, and Z. Jiang, "Decay properties of Er^{3+} ions in Er^{3+}:YAG and Er:$YAlO_3$," Physica B **324**(1-4), 43–48 (2002).
28. http://www.baikowski.com/
29. B. R. Judd, "Optical absorption intensities of rare-earth ions," Phys. Rev. **127**(3), 750–761 (1962).
30. G. S. Ofelt, "Intensity of crystal spectra of rare-earth ions," J. Chem. Phys. **37**(3), 511–520 (1962).
31. A. A. Kaminskii, *Laser Crystals, Their Physics and Properties* (Springer, 1981).
32. D. L. Dexter, "A theory of sensitized luminescence in solids," J. Chem. Phys. **21**(5), 836–850 (1953).
33. C. Wei, *Doped Nanomaterials and Nanodevices, Photonics and Nanodevices* (American Scientific Publishers, 2010).

1. Introduction

In recent years, highly transparent polycrystalline rare-earth element doped $Y_3Al_5O_{12}$ (YAG) ceramics (especially Nd: YAG) has become a significant laser media with the improved fabrication technologies and the proper diode laser excitation system. YAG single crystal has already proved its potential as a laser material especially doped with Nd^{3+} [1–3]. However, because of the difficulty to make large size single crystalline material using conventional single crystal growth methods, ceramic technology has been adopted with which one can make homogeneous large size YAG at comparatively lower cost. It has been proved that YAG ceramics materials exhibit excellent laser performance similar to YAG single crystals [3–10]. Among the rare-earth doped YAG-materials, high content Er^{3+}:$Y_3Al_5O_{12}$ (Er: YAG [10–15] single crystal and ceramics are important laser media to obtain laser emission at 3 μm, which is widely utilized by the medical community. Since this emission at 3 μm fortuitously overlaps with one of the few transition bands in the water-vapor spectrum, it is useful for meteorological applications. Laser experiment on 3 μm emission on 50% Er: YAG crystal has been reported by different groups [10–12].

Recently Zhou et al. reported the synthesis and upconversion spectral studies of Er doped YAG ceramic where the grain size was estimated to be 30 μm [13]. Upconversion spectral studies were also reported in Er and Er: Yb: YAG ceramics by other groups [14–17]. Sardar et.al. reported the optical studies and comparison of various spectroscopic parameters of high Er content (50%) YAG ceramic with low Er content single crystal YAG [18].

#150115 - $15.00 USD Received 30 Jun 2011; revised 12 Aug 2011; accepted 10 Oct 2011; published 17 Oct 2011

In this paper, we report the synthesis and spectroscopic characteristics of high Er^{3+} content (50%) transparent YAG ceramic co-doped with nominal 0.1% Cr^{3+}.The purpose of this study is to explore the near infrared emission mechanisms in Er^{3+} by pumping directly the Er^{3+} or by exciting the Cr^{3+} to its absorption band at 407 nm and utilize the purposed material as laser active medium. Introduction of Cr^{3+} was found to have influence on the emission characteristics of several rare earths such as Nd^{3+} [19–22] and Er^{3+} [23] by suitable energy transfer mechanism which is determined by the concentrations of Cr and the rare earths [19–23].

To the best of our knowledge this is the first report on the detail spectroscopic investigation of a high Er content (50%) YAG co doped with nominal Cr^{3+} (0.1 mol%).

2. Experimental

2.1 Synthesis and characterization

Transparent ceramics of Er: Cr: YAG (Er = 50% and Cr = 0.1% mol %) have been prepared by nanocrystalline assisted advanced ceramic laser technology [2], and then sliced and polished for optical measurements. The microstructure of the sample was characterized by scanning transmission electron microscope (FE-STEM) FEI Quanta 200 3D operated at 25 kV in low vacuum mode. The crystal structure of the sample has been analyzed using X-ray powder diffraction (XRD) at 40 KV and 30 mA in the parallel beam configuration using RIGAKU Ultima IV X-ray diffractometer with Cu Kα (λ = 1.5 A).

The absorption spectra were measured in the 300–1700 nm range using a UV-Vis-NIR spectrophotometer (Cary, Model 14R) in the transmission mode. The upconversion and near-infrared (NIR) emission spectra are recorded under the excitation at 967 nm band of Ti-Sapphire laser (Spectra Physics, Model 3900S) pumped by an Nd: YAG laser (Spectra Physics, Model Millennia). The NIR emission was also collected under the 407 nm excitation from a laser diode (Nichia Ltd). The emission from the sample was collected with a 1.25 m single grating scanning monochromator (SPEX, Model 1250M) and detected by a liquid nitrogen cooled InGaAs detector (DSS-1GA020L, Electrooptic System Inc) for the NIR and photo multiplier tube at –950V bias (Model 1911, Horiba) for the visible. The fluorescence spectrum for NIR transitions was scanned using a 600 grooves/mm diffraction grating blazed at 1.5 μm and 1200 grooves/mm diffraction grating blazed at 0.5 μm for the visible region, with a spectral resolution of 0.01 nm. The detector signal was processed in a computer coupled to the data acquisition system through a lock in amplifier (Stanford Research System, Model SR510,). The entire system was controlled though the data acquisition software Synerjy (Origin Lab), and HORIBA Jobin-Yvon). The decay profiles corresponding to 1571 nm, 557 nm and 680 nm were recorded by pulsing the excitation laser with a mechanical chopper (Terahertz Technology, Model C-995) and connecting the detector directly to a 155 MHz oscilloscope (Tektronix, Model 2445A). In all emission and decay experiments, the sample was excited near the surface to avoid the re-absorption losses. All the emission and decay time measurements were performed at room temperature.

3. Results and discussion

3.1. Phase and morphology

Figure 1 shows the X-ray powder diffraction patterns of transparent ceramic sintered at 1750 °C and is compared with standard JCPDS data of YAG (01-073-3184). It is clear that the patterns were basically consistent with YAG phase and no additional phases were observed. XRD results reveal that the polycrystalline transparent YAG ceramic sample has a cubic phase structure with unit cell parameters a = b = c = 11.99 Å.

Figure 2 shows the scanning electron microscope (SEM) micrograph of the ceramic with a photograph of mirror-polished Er: Cr: YAG ceramic in the inset. According to the SEM analysis, specimen is very compact and almost contains no pores. Based on SEM analysis, we

#150115 - $15.00 USD Received 30 Jun 2011; revised 12 Aug 2011; accepted 10 Oct 2011; published 17 Oct 2011

did not observe any other phases along the grain boundaries and in the inner grains. The average grain size of the Er: YAG ceramics is about 6.9 μm. Such narrow grain boundary ensures the low scattering in the material.

The mirror-polished ceramic sample of thickness 3.81 mm possesses transparency up to nearly 84% at 1571 nm with estimated scattering losses of 0.011 cm^{-1}. The reflectivity was calculated to be 0.097 (i.e.9.7%) at 1571 nm under the assumption of normal incidence.

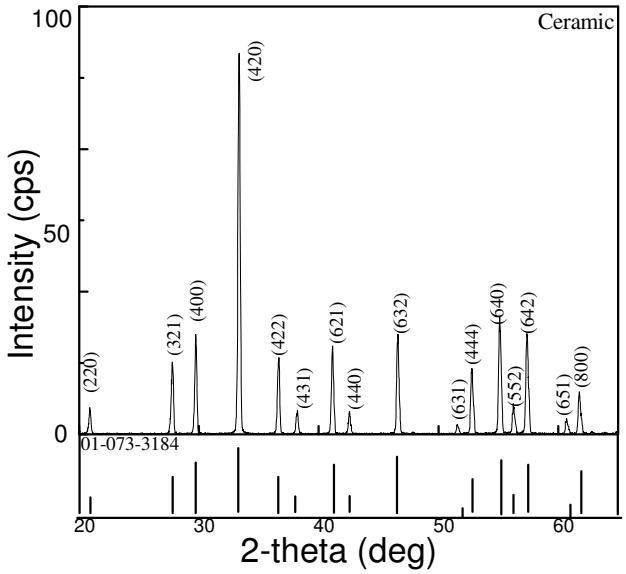

Fig. 1. X-Ray diffraction pattern of the Er: Cr: YAG ceramic.

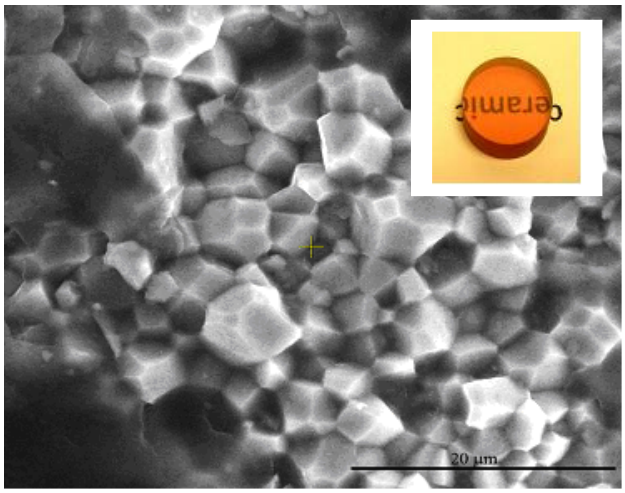

Fig. 2. Fracture surface of transparent Er: Cr: YAG ceramics showing inner grains using SEM. Inset shows the photograph of mirror-polished Er: Cr: YAG ceramic.

3.2 Radiative properties

The room temperature UV-VIS-NIR absorption spectrum of the sample is shown in Fig. 3 with their spectral band assignments. The Fresnel surface reflection losses have been subtracted in all absorption measurements. It was found that all absorption bands of Er^{3+} in this YAG host is similar to those of previously reported garnet hosts [24–27]. The spectrum is

#150115 - $15.00 USD Received 30 Jun 2011; revised 12 Aug 2011; accepted 10 Oct 2011; published 17 Oct 2011

well resolved so that almost every Stark components corresponding to different manifold of Er^{3+} are observed.

Since the concentration of Cr^{3+} is too low and its absorption bands are overlapping with Er^{3+}, it is difficult to resolve the Cr^{3+} absorption bands corresponding to $^4T_1$ at 456 nm, where the other band of Cr^{3+} corresponding to $^4T_2$ at 600 nm is absent.

The absence of Cr^{3+}absorption and emission band at 600 nm band clearly indicates that at low dopant concentration, Cr^{3+} absorption bands are either absent or totally overwhelmed by the highly doped Er^{3+} comparing with nominal presence of Cr (0.1 mol%).

The indices of refraction of the ceramic were found from [28]. A least-squares fitting to the Sellmeier's dispersion equation

$$n^2(\lambda) = 1 + \frac{S\lambda^2}{\lambda^2 - {\lambda_0}^2}, \tag{1}$$

gives values for the constants S = 2.569 and λ_0 = 172.51 nm. These constants are then used to the Eq. (1) to find the refractive indices of the YAG at all wavelengths of interest.

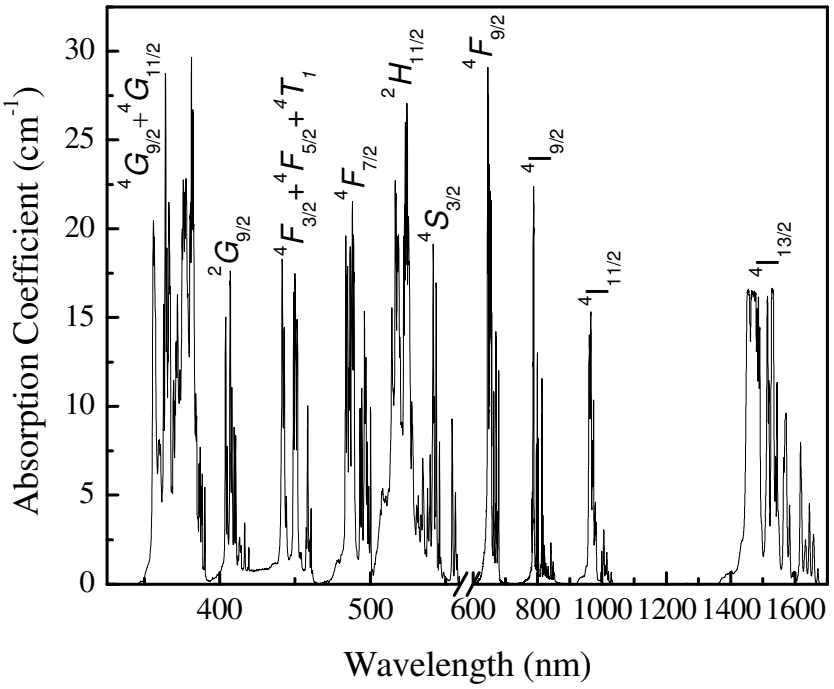

Fig. 3. Room temperature UV-VIS-NIR absorption spectrum of Cr^{3+}/Er^{3+} co-doped YAG transparent ceramic.

The absorption bands of Er^{3+} ion correspond to transitions from the $^4I_{15/2}$ ground state to the various excited levels. The data from these absorption spectra can be used to calculate the radiative transition probabilities, fluorescence branching ratios and radiative lifetimes of different transitions.

#150115 - $15.00 USD Received 30 Jun 2011; revised 12 Aug 2011; accepted 10 Oct 2011; published 17 Oct 2011

The measured absorption line strength (S_{meas}) for the electric dipole transition of each band was determined experimentally from the area under the absorption band and can be expressed in terms of absorption coefficient α (λ) by the following equation [29]:

$$S_{meas}(J \to J') = \frac{3hc(2J+1)}{8\pi^3 \lambda e^2 N_0}\left[\frac{9n}{(n^2+2)^2}\right]\int \alpha(\lambda)d\lambda. \quad (2)$$

Here, J and J` denote the total angular momentum quantum number of the initial and final states, respectively, e is the charge of the electron, c is the velocity of the light in the vacuum, h is Planck's constant, l is the mean wavelength of the absorption band and N_0 is the Er^{3+} ion concentration per unit volume, $\alpha(\lambda) = 2.303A(\lambda)/d$ is the measured absorption coefficient at a given wavelength λ, A(λ) the absorbance, d the thickness of the sample and n is the measured refractive index. The factor in bracket represents the local field correction for Er^{3+} ion in the initial J manifold. In case of most of the transitions however, the magnetic dipole contribution is zero, but in case of $^4I_{13/2} \rightarrow {}^4I_{15/2}$ transition it is significant. The values of S_{meas} obtained by the numerical integration of the absorption line shapes were used to obtain the phenomenological Judd–Ofelt parameters Ω_t (t = 2, 4, 6) by fitting the experimental value with the theoretical expression derived by Judd [29] and Ofelt [30] as

$$S_{calc}(J \to J') = e^2 \sum_{2,4,6} \Omega_t \left|\left\langle (S,L)J \left\| U^t \right\| (S',L')J' \right\rangle\right|^2. \quad (3)$$

Here, $\left\| U^t \right\|$ are the doubly reduced matrix elements of the unit tensor operator of rank t = 2, 4 and 6 which are calculated from the intermediate coupling approximation. The reduced matrix elements are virtually independent of the ligand species surrounding the rare earth ions and thus approximately unchanged from host to host. The values of these matrix elements are obtained from the published reports [31]. The three Judd–Ofelt parameters were obtained by fitting the measured dipole strength (Eq. (1)) to the theoretical dipole strength (Eq. (2)) using the least square fitting procedure. The experimental and calculated electric dipole line strengths of the different absorption bands observed are collected in Table 1 along with the RMS deviation of the fit. The calculated values of the phenomenological Judd-Ofelt parameters obtained for the Er^{3+} in the present system are $\Omega_2 = 0.42 \times 10^{-20}$ cm^2, $\Omega_4 = 0.70 \times 10^{-20}$ cm^2, $\Omega_6 = 0.47 \times 10^{-20}$ cm^2 with the RMS error of 0.047×10^{-20} cm^2. These values are in agreement with the values reported earlier for high Er doped single crystals [26] as shown in Table 2.

Table 1. Measured and Calculated Absorption Line Strengths of Er^{3+}in Cr^{3+}:Er^{3+}: YAG (Er = 50% and Cr = 0.1 mol %) Transparent Ceramic at Room Temperature

Transition (from $^4I_{15/2}$)	λ (nm)	S_{meas} (10^{-20} cm^2)	S_{calc}(10^{-20} cm^2)	$(\Delta S)^2$(10^{-40} cm^2)
$^4I_{13/2}$	1571	0.809	0.764	0.002
$^4I_{11/2}$	965	0.195	0.198	0.000
$^4I_{9/2}$	804	0.140	0.125	0.000
$^4F_{9/2}$	646	0.606	0.591	0.000
$^4S_{3/2}$	554	0.100	0.104	0.000
$^2H_{11/2}$	524	0.626	0.627	0.000
$^4F_{7/2}$	488	0.298	0.397	0.010
$^2G_{9/2}$	407	0.089	0.119	0.001

Using the Ω_t parameters the radiative transition probability (A_{rad}) from different upper states to the corresponding lower manifold states can be evaluated from the following Eq. (3) [29,30]

$$A_{rad} = \frac{64\pi^4}{3h(2J+1)\lambda^3}\left(\left[\frac{n(n^2+2)^2}{9}\right]S_{ed} + n^3 S_{md}\right). \quad (4)$$

#150115 - $15.00 USD Received 30 Jun 2011; revised 12 Aug 2011; accepted 10 Oct 2011; published 17 Oct 2011

Here, S_{ed} and S_{md} represent the predicted fluorescence line strength for the induced electric and magnetic dipole transition, respectively. S_{ed} is calculated using Eq. (2) and presents a host dependence through the Ω_t parameters. S_{md} can be calculated with the expression [29,30]:

$$S_{md} = \left(\frac{e^2 h^2}{16\pi^2 m^2 c^2} \right) \left| \left\langle (S,L)J \left\| L + 2S \right\| (S',L')J' \right\rangle \right|^2, \tag{5}$$

where the term inside the bracket represents the magnetic dipole matrix element.

The radiative lifetime (τ_r) for an excited state *(J)* is calculated by

$$\tau_r = \frac{1}{\sum A(J \to J')}, \tag{6}$$

where the sum in the denominator of Eq. (6) is taken over all terminal states *J'*.

The fluorescence branching ratios β *(J→J')* are determined from the radiative decay rates by using the following expression:

$$\beta(J \to J') = \frac{A(J \to J')}{\sum A(J \to J')} \tag{7}$$

The values of the radiative transition probability for the most common emission bands are shown in Table 3, along with the estimated fluorescence branching ratios (β) and radiative decay time (τ_{rad}).

The room temperature emission cross section (σ_e) of the intermanifold transitions can be obtained using the following expression [31]:

$$\sigma(J, J' : \nu) = \frac{\lambda^2 \beta(j, J')}{8\pi c n^2 \tau_r} g(\nu), \tag{8}$$

where λ is the peak emission wavelength, τ_r is the radiative lifetime, ν is the wave number, n is the refractive index, $\beta(J, J')$ is the fluorescence branching ratio for the transition from upper manifold *J* to lower manifold *J'*, and $g(\nu)$ is the line shape function. The line shape function is obtained from the fluorescence spectrum using the following expression:

$$g(\nu) = \frac{I(\nu)}{\int I(\nu) d\nu}, \tag{9}$$

where $I(\nu)$ is the intensity at ν. The line shape function can be found for particular transition by dividing the peak intensity $I(\nu)$ by the integrated areas of the respective fluorescence spectrum.

Using this procedure emission cross-section obtained for various observed emission bands are 2.2×10^{-20} (557 nm), 2.5×10^{-20} (680 nm) and 5.2×10^{-20} cm^2 (1571 nm). Calculated JO Parameters (Ω_t, t = 2, 4, 6), Fluorescence lifetime (τ_f), Internal quantum yield (η) are reported in Table 2. It should be noted that these values are almost in agreement with the values reported for high Er content single crystals [11,26] as shown in Table 2.

#150115 - $15.00 USD Received 30 Jun 2011; revised 12 Aug 2011; accepted 10 Oct 2011; published 17 Oct 2011

Table 2. Calculated JO Parameters (Ω_t, t = 2, 4, 6), Emission Cross-Sections (σ_e), Radiative/ Fluorescence Lifetime and Comparison with Single Crystal

Spectroscopic Parameters	Ceramic (Present Work)	Single Crystal [11,21] > 25%Er:YAG
Ω_2 (10^{-20} cm^2)	0.42	0.32
Ω_4 (10^{-20} cm^2)	0.70	0.83
Ω_6 (10^{-20} cm^2)	0.47	0.51
σ_e (10^{-20} cm^2) (1571 nm)	5.2	4.0
σ_e (10^{-20} cm^2) (557 nm)	2.2	1.9
σ_e (10^{-20} cm^2) (680 nm)	2.5	2.1
τ_f (ms) 1571 nm	4.81	4.19
τ_{rad}^{calc} (ms) 1571 nm	8.46	6.8
τ_{rad}^{calc} (ms) 557 nm	1.092	0.857
τ_{rad}^{calc} (ms) 680 nm	1.065	0.883
η (1571 nm) (Internal QY)	56%	61%

Table 3. Predicted Fluorescence Line Strengths (S_{cal}), Radiative Decay Rates (A_{rad}), and Branching Ratios ($\beta_{JJ'}$) of Cr^{3+}: Er^{3+}: YAG (Er = 50% and Cr = 0.1% mol %) Transparent Ceramic at 300 K

Transition	λ(nm)	n	S_{calc} (10^{-20} cm^2)	A_{rad} (s^{-1})	$\beta_{JJ'}$	τ_{rad} (ms)
$^4I_{13/2} \rightarrow {}^4I_{15/2}$	1571	1.81	1.424	*118.20	1.000	8.460
$^4I_{11/2} \rightarrow {}^4I_{13/2}$	2778	1.78	0.644	9.73	0.122	
$^4I_{15/2}$	990	1.81	0.198	69.82	0.878	12.570
$^4I_{9/2} \rightarrow {}^4I_{11/2}$	4651	1.74	0.108	0.38	0.003	
$^4I_{13/2}$	1739	1.80	0.345	26.30	0.215	
$^4I_{15/2}$	816	1.82	0.125	95.51	0.782	8.184
$^4F_{9/2} \rightarrow {}^4I_{9/2}$	3448	1.77	0.070	0.65	0.001	
$^4I_{11/2}$	1980	1.80	0.641	32.90	0.035	
$^4I_{13/2}$	1156	1.81	0.145	38.05	0.041	
$^4I_{15/2}$	660	1.83	0.591	867.15	0.924	1.065
$^4S_{3/2} \rightarrow {}^4F_{9/2}$	3125	1.78	0.013	0.40	0.000	
$^4I_{9/2}$	1639	1.80	0.175	39.47	0.043	
$^4I_{11/2}$	1212	1.81	0.038	21.50	0.023	
$^4I_{13/2}$	844	1.81	0.163	175.79	0.192	
$^4I_{15/2}$	545	1.83	0.104	678.29	0.741	1.092

*Including the magnetic dipole transition probability A_{md} = 48.20 s^{-1}

3.3. Infrared and upconversion luminescence spectra

Figure 4 and Fig. 5 shows the near-infrared emission (NIR) of the transparent ceramic composition under the 407 and 967 nm excitation, where NIR emission was observed centered at 1571 nm with a spectral bandwidth of 300 nm. The spectra reported in Fig. 4 are in different scale to show the difference in fluorescence intensity under 967 and 407 nm excitation. Spectrum in Fig. 4 also shows that fluorescence intensity under 967 nm excitation is more than the 407 nm excitation under the identical measurement condition with the same power (60 mW), which is due to the larger excited state non-radiative losses at 407 nm excitation. As a whole fluorescence spectrum obtained under 407 nm and 967 nm excitation are shown in Fig. 5 and Fig. 6 respectively. The intense upconversion emission bands as

#150115 - $15.00 USD Received 30 Jun 2011; revised 12 Aug 2011; accepted 10 Oct 2011; published 17 Oct 2011

shown in Fig. 6 were observed at 545 nm (green), 557 nm (green), 656 nm (red), 674 nm (red), and 680 nm (red) under 967 nm excitation; which are assigned to the $^2H_{11/2} \rightarrow {}^4I_{15/2}$, $^4S_{3/2} \rightarrow {}^4I_{15/2}$, $^4F_{9/2} \rightarrow {}^4I_{15/2}$ transitions and their Stark components to ground state respectively. Green emission centered at 557 nm has been observed under the 407 nm excitation, where the red emission is absent in the spectrum as shown in Fig. 5. The fluorescence branching ratios of the upconversion bands are 15% (545 nm), 37% (557 nm) and 48% (680 nm) respectively.

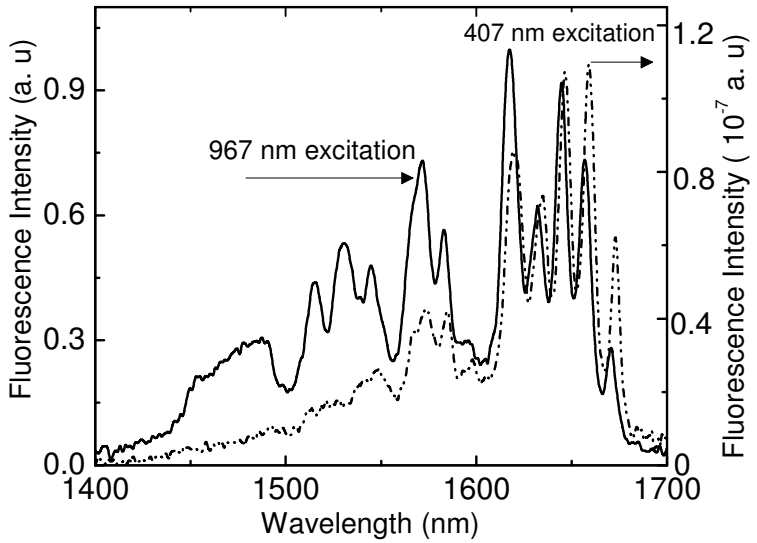

Fig. 4. Room temperature fluorescence spectra of the $^4I_{13/2} \rightarrow {}^4I_{15/2}$ transition of Er^{3+}: YAG under 967 and 407 nm excitation.

The mechanisms for the IR and upconversion visible emission bands under different excitation wavelength are explained with the help of the energy level diagram shown in Fig. 7. The process of both visible emissions can be explained on the basis of various mechanisms such as two photon absorption (TPA), excited state absorption (ESA), and energy transfer (ET). TPA is a nonlinear process where the visible photons are created by the simultaneous absorption of two IR photons and mediated through a real or virtual intermediate level. TPA is relevant when excitation light sources used have high power that is sufficiently enough to create virtual intermediate levels in materials with high TPA cross section. In the case of trivalent Er^{3+}, TPA can occur through the real state $^4I_{11/2}$ because of the presence of such matching energy level. When the $^4I_{11/2}$ level is excited by 967 nm directly through Er^{3+}, part of the excitation energy at the $^4I_{11/2}$ level relaxes non-radiatively to the $^4I_{13/2}$ level. The radiative transition via $^4I_{13/2} \rightarrow {}^4I_{15/2}$ leads to a NIR intense emission centered at 1571 nm emission.

#150115 - $15.00 USD Received 30 Jun 2011; revised 12 Aug 2011; accepted 10 Oct 2011; published 17 Oct 2011

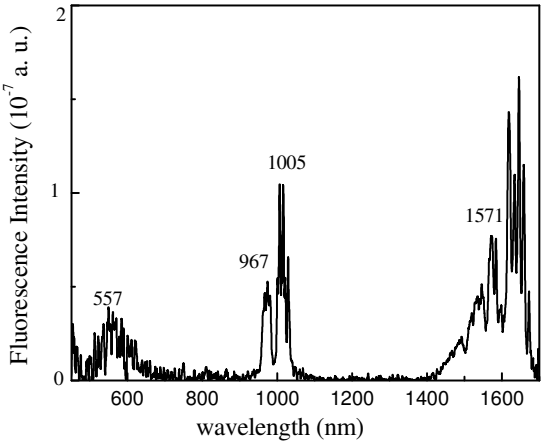

Fig. 5. Fluorescence spectrum of the ceramic under 407 nm excitation.

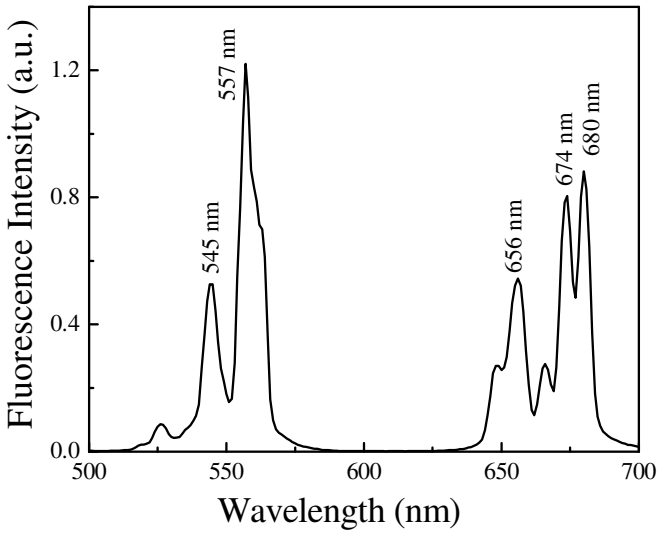

Fig. 6. Upconversion spectrum of the ceramic under 967 nm excitation.

At the same time, $^4F_{7/2}$ is populated through $^4I_{11/2}$ by TPA process. Since the lifetime of $^4I_{11/2}$ level of Er^{3+} in ceramic is high as reported in Table 3, which is enough and efficient for TPA process. The populated $^4F_{7/2}$ then relaxes non-radiatively to the next lower $^2H_{11/2}$ giving rise to the green emission at 545 nm through the $^2H_{11/2} \rightarrow {}^4I_{15/2}$ transition. Part of the population accumulated in the $^4S_{3/2}$ level through non-radiative decay from $^2H_{11/2}$ relaxes to the $^4I_{15/2}$ through the radiative decay giving the emission band at 557 nm.

In high Er content sample the green emission is also influenced due to the energy transfer (ET) as illustrated in the energy level diagram. Two erbium ions interacting as follows under 967 nm excitation: $^4I_{11/2}$ (Er^{3+}) + $^4I_{11/2}$ (Er^{3+}) $\rightarrow$ $^4F_{7/2}$ (Er^{3+}) + $^4I_{15/2}$ (Er^{3+}) contribute greatly to populating the $^4F_{7/2}$ level. The red emission is mainly due to the cross relaxation and energy transfer process according to the equation $^4I_{11/2}(Er^{3+})$ + $^4I_{13/2}(Er^{3+}) \rightarrow {}^4I_{15/2}(Er^{3+})$ + $^4F_{9/2}(Er^{3+})$.

#150115 - $15.00 USD Received 30 Jun 2011; revised 12 Aug 2011; accepted 10 Oct 2011; published 17 Oct 2011

Ultimately all these mechanisms lead to the radiative transition from the $^2H_{11/2}$, $^4S_{3/2}$ and $^4F_{9/2}$ to the $^4I_{15/2}$ level which emits green at 545 nm, 557 nm and red at 680 nm respectively. The absence of red emission under 407 nm excitation as shown in Fig. 5 also confirms that energy transfer and cross relaxation are the required and dominant phenomena for the red emission process.

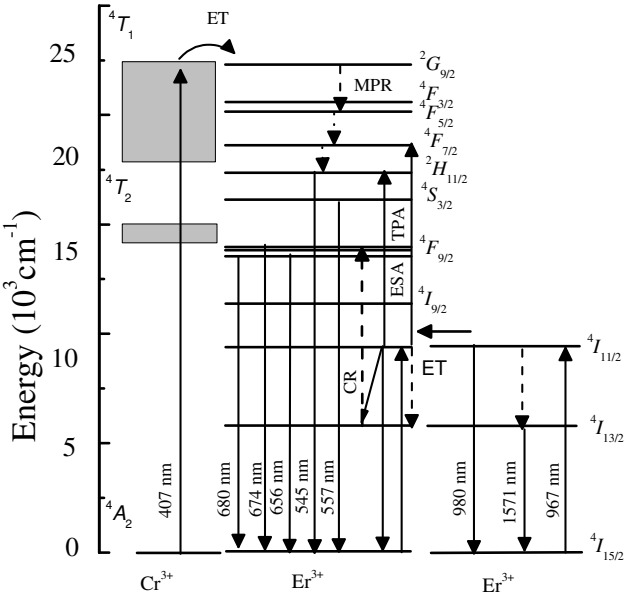

Fig. 7. Energy level diagram of Cr, Er system showing the possible excitation and de-excitation mechanisms under 407 and 967 nm. TPA- Two photon absorption; ET Energy transfer. ESA-excited state absorption; CR Cross relaxation.

In order to understand the contribution of the two-photon process we studied the pump power dependence of the green and red emission intensity. In an upconversion mechanism, the emission intensity I_{up} is proportional to the n^{th} power of the excitation intensity P i.e., $I_{up} \propto P^n$, where n is the number of IR photons absorbed to produce an up-conversion photon. A plot of log I_{up} vs. log P yields a straight line with slope n and is shown in Fig. 8 for the most intense 557 and 680 nm upconversion emissions. The values of the slopes obtained are 1.7 and 1.9 for the respective intense green and red bands, which confirms the two-photon contribution to the red and green emissions.

#150115 - $15.00 USD Received 30 Jun 2011; revised 12 Aug 2011; accepted 10 Oct 2011; published 17 Oct 2011

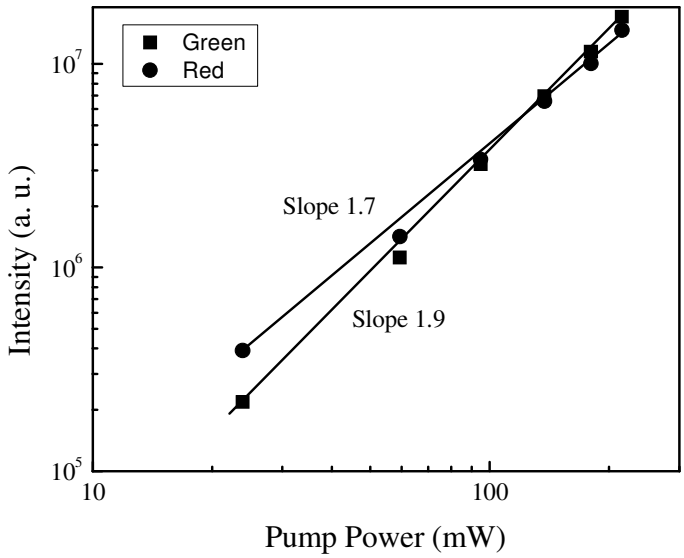

Fig. 8. Dependence of upconversion intensity on pump power density under 967 nm excitation.

3.4 Non radiative processes and internal quantum yield

Figure 9 shows the decay profiles for the 1571 nm emission of ions in the highly Er^{3+} doped transparent ceramic fitted by single exponential function with a correlation factor of 0.99998 under 967 nm excitation. Figure 10 shows the semi-log plot for the decay profile for 557 and 680 nm of Er^{3+} ions in the co-doped sample.

A quantitative way of measuring the internal quantum yield (η) for a particular emission band is done through the fluorescence lifetime measurements. Non-radiative processes such as multiphonon relaxation, vibrational losses by hydroxyl and other functional groups and energy transfer interaction quench the fluorescence intensity and the efficiency. The observed lifetime of the emission can be written as [32]

$$\frac{1}{\tau_f} = A_{rad} + W_{mp} + W_{OH} + W_{ET}, \tag{10}$$

where A_{rad}, W_{mp}, W_{HO}, W_{ET} are respectively the radiative transition rate, transition rate from multiphonon relaxation, hydroxyl groups and energy transfer interactions respectively. The main contribution to non-radiative decay for the sample with high dopant comes from multiphonon relaxation from the host and energy transfer interaction between nearby ions.

The internal quantum efficiency (η) can be evaluated from the ratio of the fluorescence to radiative decay time [33]. The fluorescence lifetime obtained for the 1571 nm emission in the present transparent ceramic composition was 4.81 ms, which is within the range of fluorescence lifetime observed for single crystal viz. 7.14 ms at 40 mol. % and 1.95 ms at 60 mol % [11]. The decay time for the present sample is as expected with high dopant concentration, where rate of migration of the excitation energy is dominant. With the calculated radiative decay time of 8.46 ms, a radiative internal quantum efficiency of 56% was obtained for the Er (50%) Cr (0.1%) YAG ceramic sample. Similarly the fluorescence lifetime for green (557 nm) and red (680 nm) were measured to be 265 μs (± 0.124 μs) and 264 μs (± 0.126 μs) with internal quantum efficiency 24.8% and 24.17% respectively. However the influence of other non-radiative interactions detracts the efficiency less than

#150115 - $15.00 USD Received 30 Jun 2011; revised 12 Aug 2011; accepted 10 Oct 2011; published 17 Oct 2011

100% as noticed in other samples. The higher value of calculated radiative lifetime was expected in the highly Er (50%) doped YAG ceramic compared to 29% Er doped single crystal as reported in Table 2.

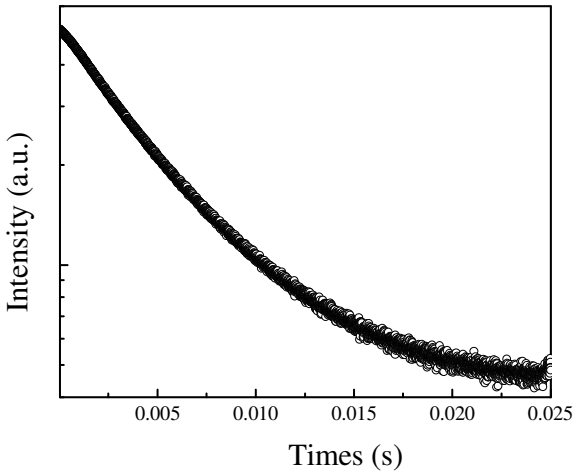

Fig. 9. Decay profile of 1571 nm NIR emission under 967 nm excitation.

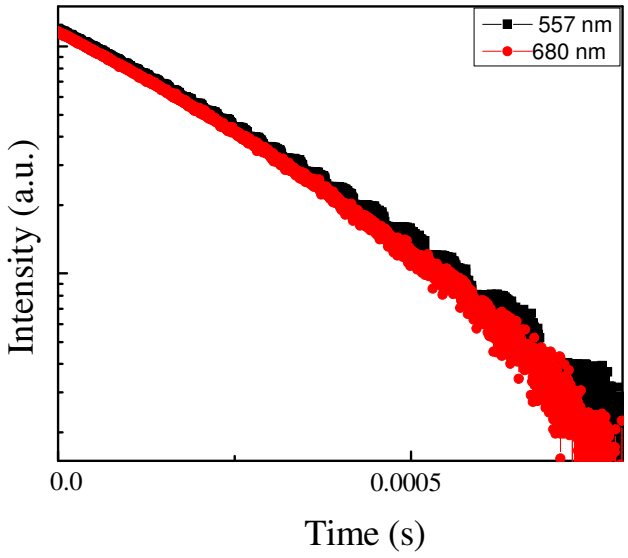

Fig. 10. Decay profile of 557 nm and 680 nm visible emissions under 967 nm excitation.

4. Conclusion

We performed experiments for characterizing the Er: Cr: YAG (Er = 50% and Cr = 0.1% mol %) doped transparent YAG ceramic structurally, optically and compared with Er^{3+} doped single crystal. SEM measurement shows that the average grain size is 6.9 μm. Various spectroscopic parameters such as Judd-Ofelt parameters, emission cross sections, branching ratios, etc. determined for the transparent ceramic sample are very much similar to high Er

#150115 - $15.00 USD Received 30 Jun 2011; revised 12 Aug 2011; accepted 10 Oct 2011; published 17 Oct 2011

content YAG single crystal samples. The internal quantum yield for NIR (1571 nm), green (557 nm), and red (680 nm) were calculated to be 56%, 24.8%, and 24.17% respectively for Er: Cr: YAG ceramic. The fluorescence lifetime for the transition $^4I_{13/2} \rightarrow {}^4I_{15/2}$ (Er^{3+}) is 4.81 ms, which is more than the 60% Er^{3+} doped YAG but less than 40% Er^{3+} doped YAG single crystal. The short florescence lifetime for the highly doped sample was as expected where various non-radiative processes are more dominant such as energy transfer. Because of the low concentration, the effect of Cr^{3+} (0.1%) as a sensitizer ion was not prominent.

Acknowledgments

This work was supported by the National Science Foundation Partnerships for Research and Education in Materials (PREM) Grant No. DMR-0934218.

#150115 - $15.00 USD Received 30 Jun 2011; revised 12 Aug 2011; accepted 10 Oct 2011; published 17 Oct 2011